Nanoscale

PAPER

Cite this: DOI: 10.1039/c5nr05645d

Tunable multiband metasurfaces by moiré nanosphere lithography†

Zilong Wu,‡[a] Kai Chen,‡[b,c] Ryan Menz,[a] Tadaaki Nagao*[b,c] and Yuebing Zheng*[a]

Moiré nanosphere lithography (MNSL), which features the relative in-plane rotation between two layers of self-assembled monodisperse nanospheres as masks, provides a cost-effective approach for creating moiré patterns on generic substrates. In this work, we experimentally and numerically investigate a series of moiré metasurfaces by MNSL. Due to the variety of gradient plasmonic nanostructures in arrays, single moiré metasurfaces can support multiple localized surface plasmon (LSP) modes with a wide range of resonant wavelengths from ~600 nm to ~4200 nm. We analyze the origin of the LSP modes based on the optical spectra and near-field electromagnetic distributions. In addition, we fabricate and analyze the metasurfaces with high-density nanogap structures. These nanogap structures support plasmonic gap modes with significant field enhancements. With their tunable multiband optical responses from visible to near-infrared to mid-infrared regimes, these moiré metasurfaces are applicable for ultrabroadband absorbers, multiband surface-enhanced infrared and Raman spectroscopy, and broadband single-molecule spectroscopy.

Received 19th August 2015,
Accepted 19th September 2015
DOI: 10.1039/c5nr05645d
www.rsc.org/nanoscale

Introduction

With the capability of manipulating light beyond the diffraction limit at excitation of surface plasmons (SPs), the light-coupled coherent oscillation of the electron clouds in metals, plasmonic nanostructures have enabled numerous applications, including sensors,[1–6] plasmonic lenses,[7,8] light emitting diodes,[9–11] and super absorbers.[12–14] Recent years have witnessed great interest in metasurfaces for flat optics, where the designed two-dimensional arrangements of plasmonic nanostructures exhibit intriguing light-manipulation capabilities beyond the individual nanostructures.[15–22] A variety of metasurfaces consisting of plasmonic nanostructures with various shapes, sizes, and arrangements have been demonstrated for applications in solar energy conversion,[23–25] analog computing,[26–28] and optical filters.[29] However, the large-scale implementation of these metasurfaces has remained challenging because current nanofabrication methods such as electron beam lithography and focused ion beam lithography are both time-consuming and high-cost.

Self-assembly methods such as block copolymer lithography[30] and nanosphere lithography (NSL)[31–33] are emerging as promising approaches towards cost-effective, large-scale fabrication of nanostructures. However, most of the self-assembly methods can only fabricate simple periodic patterns of plasmonic nanostructures with a single type of shape and size, significantly limiting the bandwidth, the light-manipulation capability, and thus applications of the metasurfaces. For example, applications in solar-energy harvesting and multiband surface-enhanced infrared absorption (SEIRA) spectroscopy and surface-enhanced Raman spectroscopy (SERS) prefer to use metasurfaces with broadband field enhancements, which require an increased complexity in the arrangements of plasmonic nanostructures with different shapes and sizes that support multiple SP modes in a broad range of wavelengths.[17,34]

Recently, several NSL variations, where either the layers of monodisperse spheres or the metal deposition processes are altered from the conventional methods, have exhibited potential for increasing the complexity of plasmonic nanostructures and their spatial arrangements for function-enhanced metasurfaces.[35,36] In particular, moiré nanosphere lithography (MNSL),[36] which utilizes two stacked layers of polystyrene (PS) nanospheres as etching and metal deposition masks, provides a cost-effective, high-throughput method to create metasurfaces with moiré patterns. Moiré metasurfaces that feature a large number of component sets and high rotational

[a]Department of Mechanical Engineering, Materials Science and Engineering Program, and Texas Materials Institute, The University of Texas at Austin, Austin, Texas 78712, USA. E-mail: zheng@austin.utexas.edu
[b]International Center for Material Nanoarchitectonics (MANA), National Institute for Materials Science, Tsukuba, 305-0044, Japan. E-mail: Nagao.Tadaaki@nims.go.jp
[c]CREST, Japan Science and Technology Agency, 4-1-8 Honcho, Kawaguchi, Saitama, 332-0012, Japan

†Electronic supplementary information (ESI) available: Methods of optical measurements and simulations. Near-field optical spectra of the nanogaps. See DOI: 10.1039/c5nr05645d

‡These authors contribute equally to this manuscript.

symmetry are promising candidates to achieve broadband field enhancements.[37]

In this work, we experimentally and theoretically investigate the optical properties of the moiré metasurfaces created by MNSL. The in-plane angle of rotation between the two PS monolayers is controlled to create a series of moiré metasurfaces with tunable sets of plasmonic nanostructures that support variable localized surface plasmon (LSP) modes. We observe that single metasurfaces exhibit multiple LSP modes that cover a wide range of response wavelengths from ~600 nm to ~4200 nm. We also control the optical responses of the metasurfaces by using PS nanospheres of different sizes. Moreover, MNSL can be precisely tuned to give rise to high-density nanogap structures with reproducible gap sizes smaller than 50 nm. The high tunability of the LSP modes and the multiband optical responses make the moiré metasurfaces highly suitable for broadband light harvesting and ultrahigh-sensitive SERS that features simultaneous enhancements of both the excitation and emission processes. Due to the highly enhanced local fields at the excitation of plasmonic gap modes, moiré metasurfaces with nanogap structures are promising for single-molecule surface-enhanced spectroscopy. With its cost effectiveness and high throughput in combination with the tunable multiband properties of the moiré metasurfaces, MNSL will help to speed up the large-scale implementation of metasurfaces in practical applications.

Fabrication of moiré metasurfaces by MNSL

The moiré metasurfaces were fabricated using MNSL as illustrated in Fig. 1(a). Two layers of PS nanospheres with relative in-plane rotation are formed on a glass substrate followed by metal deposition and selective removal of PS.[36] In brief, PS nanospheres were self-assembled at the water–air interface to form the monolayers, and subsequent water withdrawal transfers the monolayer onto a glass substrate submerged in water. A second PS monolayer is deposited on top of the first monolayer *via* the same process. The stacking pattern of the PS bilayer is tunable by the relative rotation angle (θ) between the top and bottom PS monolayers. Next, O_2 reactive ion etching (RIE) is applied to reduce the size of the PS nanospheres. The etched bilayer works as a mask for metal deposition. Au is deposited onto the glass substrate through the interstices within the mask using a thin layer of Cr as an adhesion layer. Lastly, ultrasonication of the substrate in toluene is applied to selectively remove the PS nanospheres and metal on the top, leaving the Au moiré metasurface on the glass substrate. Tuning θ leads to the precise control of the moiré patterns. We can also use different types of PS nanospheres to tune the metasurfaces. Therefore, MNSL has a remarkable flexibility in creating moiré metasurfaces with tunable patterns.

Fig. 1(b) and (c) show the scanning electron microscopy (SEM) images of two representative Au moiré metasurfaces. The size of the PS nanospheres is 510 nm. The thickness of the Au is 50 nm. These two metasurfaces were created based on the different rotation angles ($\theta \sim 12°$ for Fig. 1b and $\theta \sim 19°$ for Fig. 1c) between the two PS monolayers in MNSL. Both metasurfaces exhibit a certain level of rotational symmetry and periodicity with different unit cells. The unit cell in Fig. 1(b) consists of hole arrays, triangles, and z-shaped structures, while the unit cell in Fig. 1(c) consists of ring-like structures surrounded by several z-shaped structures. The smallest feature size for the metasurfaces is ~250 nm. We can further reduce the smallest feature size by reducing O_2 RIE time and/or using PS nanospheres of smaller diameters. For example, we achieved the smallest feature size of ~160 nm when 300 nm PS nanospheres were used. However, the synthesis and self-assembly become more challenging for PS nanospheres of small diameters, increasing the defects of the metasurfaces.

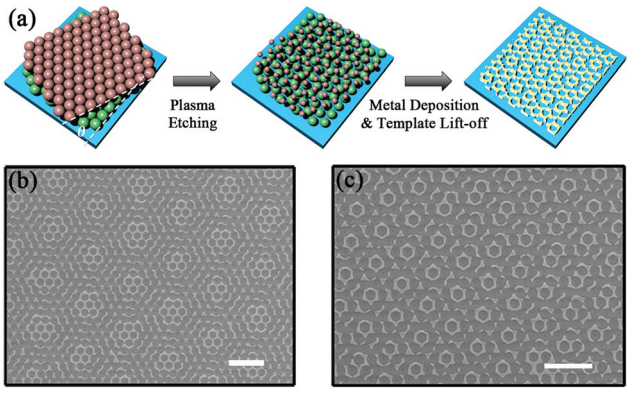

Fig. 1 (a) Schematic of fabrication of moiré metasurfaces by MNSL. θ indicates the angle of in-plane rotation between the two layers of self-assembled monodisperse PS spheres. SEM images of two representative moiré metasurfaces with $\theta \sim 12°$ (b) and $\theta \sim 19°$ (c), respectively. The scale bars in (b) and (c) are 2 μm.

Results and discussion

At the top of Fig. 2(a), we show the measured and simulated transmission spectra of a Au moiré metasurface with $\theta \sim 19°$

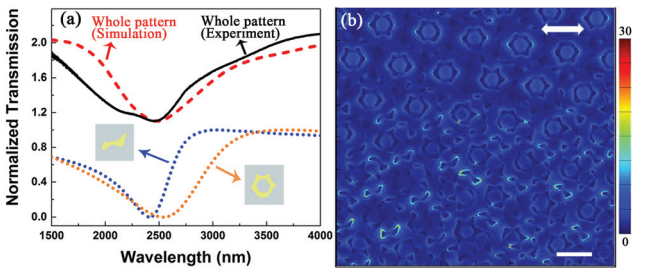

Fig. 2 (a) Top: normalized transmission spectra of the Au metasurface in Fig. 1(c). Bottom: simulated transmission spectra for two types of Au nanostructures that dominate the metasurface. The simulations are based on single nanoparticles. (b) The spatial distributions of the electric field amplitude on the metasurface at a wavelength of 2500 nm (*i.e.*, around the dips in the transmission spectra in Fig. 2(a). The white arrow represents the polarization of the incident light. The scale bar is 1 μm.

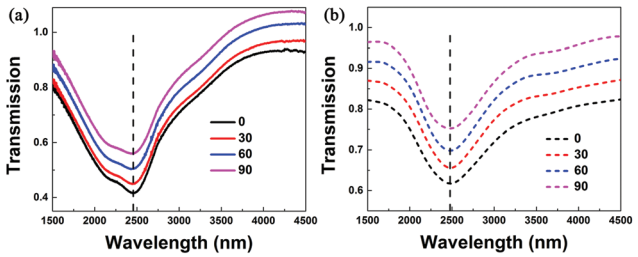

Fig. 3 (a) Measured and (b) simulated transmission spectra of the metasurface in Fig. 1(c) with incident light of variable polarizations from 0° to 90° at intervals of 30°. The polarization indicated in Fig. 2(b) is regarded as 0°. For clarity, the transmission spectra are offset vertically.

in the mid-infrared (MIR) regime (Fig. 1c). The ESI† includes the details on the optical measurements and simulations. Both spectra exhibit transmission dips at a wavelength of ~2500 nm. To understand the nature of these dips, we map the electromagnetic field distributions on the metasurface at the wavelength of 2500 nm. As shown in Fig. 2(b), strong electrical field enhancements occur at two types of Au nanostructures: the ring-like nanostructures and the z-shaped nanostructures. We further simulated the transmission spectra for these two types of nanostructures. As shown at the bottom of Fig. 2(a), both nanostructures exhibit the transmission dips around the wavelength of 2500 nm despite their different shapes. The dips arise from the plasmonic dipole modes. Specifically, the ring and z-shaped nanostructures have resonant peak wavelengths at 2540 nm and 2410 nm, respectively, which agrees with the experimental spectrum of the metasurface where two dips occur at 2480 nm and 2200 nm, respectively.

It is worth noting that the arrangements of both types of Au nanostructures on the metasurface exhibit a high rotational symmetry (Fig. 1c). We hypothesize that the symmetry can lead to a polarization-independent optical response of the metasurface. To test this hypothesis, we measured and simulated transmission spectra of the metasurface under incident light with variable polarizations from 0° to 90° (Fig. 3). We can see that both the shape and dip wavelength of the transmission spectra remain unchanged when the polarization of the incident light is changed from 0° to 90° at intervals of 30°. The polarization independence is beneficial to applications such as solar energy conversion.

MNSL is versatile in tuning the metasurfaces by simply controlling the angle of rotation (θ) between the top and bottom nanosphere monolayers. At the top of Fig. 4(a), we show the simulated and experimental transmission spectra of a Au metasurface with $\theta \sim 7.5°$ in the MIR regime. Different from those of the metasurface with $\theta \sim 19°$, both spectra exhibit two transmission dips at the wavelengths of ~2500 nm and ~4200 nm. To understand the origin of these dips, we map the spatial distributions of the electric near-field amplitude at these two dips. As shown in Fig. 4(b) and (c), the z-shaped nanostructures of different lengths are optically excited at

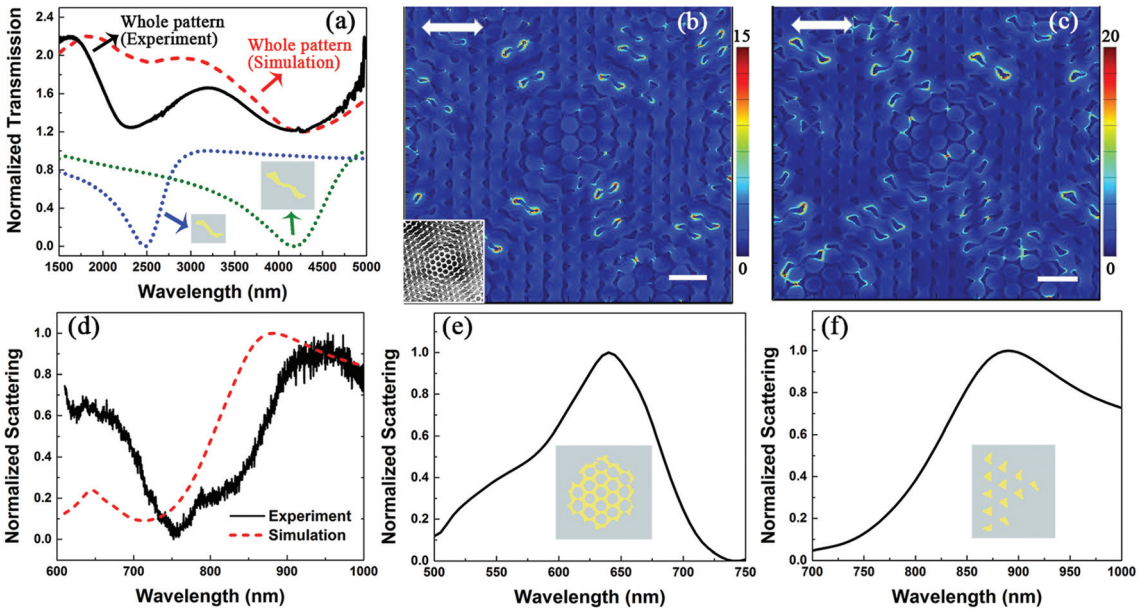

Fig. 4 (a) Top: measured and simulated transmission spectra of the Au metasurface by MSNL with a θ of ~7.5°. Bottom: simulated transmission spectra for short (blue dotted line) and long (green dotted line) z-shaped nanostructures as individuals. (b & c) Spatial distributions of the electric field amplitude on the metasurface at the wavelengths of 2500 nm and 4200 nm. The arrows indicate the polarization of the incident light. The scale bars are 1 μm. The inset of (b) shows the SEM image of a unit cell of this metasurface. (d) Measured and simulated scattering spectra of the metasurface in the visible and near infrared (NIR) regimes. (e) Simulated scattering spectrum of the nanohole array part in the metasurface. The inset shows the schematic of the Au nanohole array used in the simulation. (f) Simulated scattering spectrum of the Au nanotriangle array part of the metasurface. The inset shows the schematic of the Au nanotriangle array used in the simulation.

these two wavelengths. The incident light of 2500 nm excites the z-shaped nanostructures with a length of ~625 nm while the light at 4200 nm excites the nanostructures with a longer length of ~1100 nm. From the electric field distributions, we identify that both excitations arise from the plasmonic dipole modes.

To further confirm the origin of these two transmission dips, we simulated the transmission spectra of the short and long z-shaped nanostructures as individuals. As shown at the bottom of Fig. 4(a), the short and long nanostructures exhibit the transmission dips at 2500 nm and 4200 nm, respectively, which match well with the two dips in the transmission spectra of the metasurface. The spectral match confirms that the optical response of the metasurface in the infrared wavelength regime arises from the plasmonic dipole modes of the two types of z-shaped nanostructures. Unlike the two closely positioned resonant wavelengths in Fig. 2(a), the resonant wavelengths in Fig. 4(a) are separated by 1700 nm.

As shown in Fig. 4(b) and (c), the triangular nanostructures and nanohole arrays are not excited in the MIR regime. To reveal the plasmonic modes for these two types of nanostructures, we experimentally and theoretically investigate the optical responses of the metasurface in the visible and near-infrared (NIR) regimes. Dark-field scattering spectroscopy was employed for the measurements. As shown in Fig. 4(d), both experimental and simulated spectra exhibit two scattering peaks at ~640 nm and ~900 nm. The slight mismatch between these two spectra can be attributed to the fact that the dark-field scattering setup used non-normal incident light while normal incident light was used in the simulation. The scattering simulations for the Au nanotriangle and nanohole arrays, as shown in Fig. 4(e) and (f), reveal that the scattering peaks at 640 nm and 890 nm arise from the nanohole and nanotriangle arrays, respectively. These two peaks match well with those in the spectra from the metasurface (*i.e.*, whole pattern) in Fig. 4(d). Therefore, the metasurface supports multiple LSP modes in a wide range of wavelengths from visible to MIR, which is particularly attractive for applications in ultrabroadband light absorbers and multiband SERS-SEIRA substrates.[38,39]

Another effective way to tune the metasurfaces by MNSL is to change the size of the PS nanospheres. We comparatively studied the metasurfaces based on 510 nm and 300 nm PS nanospheres. Fig. 5(a) and (b) show the SEM images of the Au metasurfaces with $\theta \sim 7.5°$ using 510 nm and 300 nm nanospheres. Both metasurfaces consist of four types of nanostructures: nanohole arrays, nanotriangle arrays, short z-shaped nanostructures, and long z-shaped nanostructures. We measured and simulated scattering spectra of the metasurfaces in visible and NIR regimes, as shown in Fig. 5(c) and (d). From both the experimental and simulated spectra, we can see that the scattering spectra of these two metasurfaces exhibit similar features with two scattering peaks, which blue-shift when the PS nanospheres are reduced from 510 nm to 300 nm. The scattering peaks at the short and long wavelengths arise from the nanohole and nanotriangle arrays, respectively. Therefore, MNSL is effective in fabricating variable moiré metasurfaces by controlling the angle of rotation between the two layers of PS nanospheres and the size of PS nanospheres.

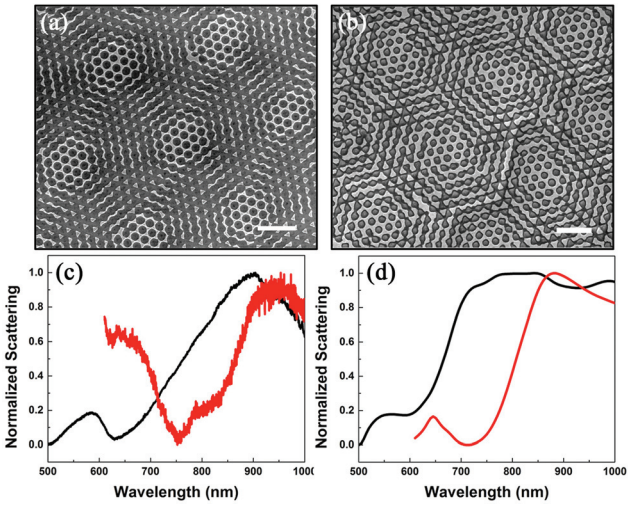

Fig. 5 SEM images of the Au metasurfaces with $\theta \sim 7.5°$ using (a) 510 nm and (b) 300 nm PS nanospheres. The scale bars in the images are 2 μm (a) and 1 μm (b). (c) Measured and (d) simulated scattering spectra of the metasurfaces using 510 nm (red lines) and 300 nm (black lines) PS nanospheres.

We further demonstrate that MNSL can fabricate metasurfaces with arrays of sub-50 nm nanogaps. These nanogaps support "hot spots" with significant field enhancements. Fig. 6(a) shows such a metasurface when θ is around 16°. We focus on investigating two types of nanogaps in the metasurface by simulating their optical spectra and near-field electromagnetic distributions. One is the fan-like nanostructure. As shown in Fig. 6(b) and (c), the fan-like nanostructure exhibits tunable "hot spots" depending on the polarization and wavelength of the incident light. In Fig. 6(b), a plasmonic dipole mode of the nanogap, similar to the gap modes in the well-studied bowtie nanostructures,[40] is excited at the wavelength of 1240 nm and the polarization is indicated by the arrow. The distributions and intensities of the "hot spot" change when the incident light of 3180 nm is polarized along another direction indicated by the arrow (Fig. 6c). We identify the plasmonic resonance wavelengths for the "hot spots" by calculating the near-field optical spectra of the nanostructures. Fig. S1(a) and (b)† show the spectra for the fan-like nanostructures within two wavelength regimes (*i.e.*, visible-NIR and MIR) at different polarizations of incident light. Due to the complexity of the fan-like nanostructures, multiple LSP modes appear in the near-field optical spectra.

The other is the split-ring nanostructures. Based on the optical spectra shown in Fig. S1(c) and (d),† we map the near-field electrical distributions at the split-ring nanostructure at the wavelengths of 790 nm, 1280 nm, and 2320 nm with controllable polarizations. As shown in Fig. 6(d)–(f), the "hot spots" arise from the different orders of the LSP modes. With

View Article Online
DOI: 10.1039/C5NR05645D
Paper

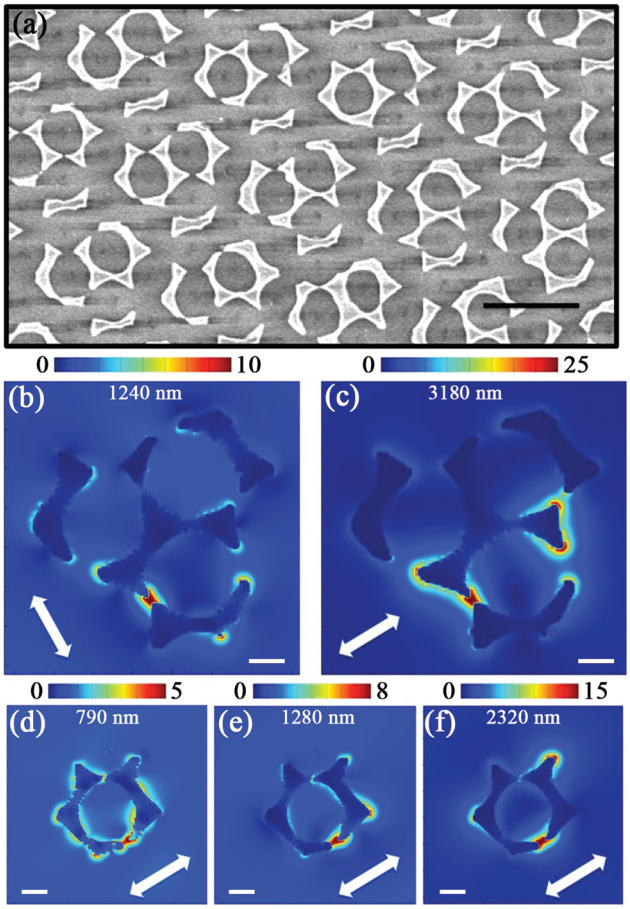

Fig. 6 (a) SEM image of the metasurface with different types of nanogaps. The scale bar is 1 μm. (b & c) Near-field electrical distributions at the fan-like nanostructure under incident light of 1240 nm and 3180 nm, respectively. The polarizations of the incident light are indicated by the arrows. The scale bars are 200 nm. (d–f) Near-field electrical distributions at the split-ring nanostructure under incident light of 790 nm, 1280 nm, and 2320 nm, respectively. The polarizations of incident light are indicated by the arrows. The scale bars are 200 nm.

their high tunability in resonance wavelengths and their strong field enhancements, these metasurfaces with a number of nanogaps have potential for multiband single-molecule spectroscopy.[41–43]

Conclusion

MNSL provides a cost-effective, high-throughput method for the fabrication of tunable multiband metasurfaces. Our experimental and theoretical studies reveal that we can tune the metasurfaces by controlling the angle of rotation between the two layers of the monodisperse PS nanospheres and the size of the PS nanospheres. We expect that more complex metasurfaces are achievable by further extending MNSL with methods such as angle-variable metal deposition and nanosphere etching. With their unique optical properties, these metasurfaces will find various applications. The multiple LSP modes in a wide range of wavelengths from visible to NIR to MIR will enable the development of ultrabroadband absorbers and multiband SERS-SEIRA substrates for ultrahigh-sensitive detection of molecules. The metasurfaces with a large number of nanogaps have potential applications in broadband single-molecule spectroscopy.

Conflict of interest

The authors declare no competing financial interest.

Acknowledgements

The authors acknowledge the financial support of the Beckman Young Investigator Program, and the Texas Advanced Computing Center (TACC) at The University of Texas at Austin for providing high performance computing (HPC) resources that have contributed to numerical simulations. URL: http://www.tacc.utexas.edu.

References

1 L. Polavarapu, J. Pérez-Juste, Q.-H. Xu and L. M. Liz-Marzán, *J. Mater. Chem. C*, 2014, **2**, 7460–7476.
2 S. Abalde-Cela, C. Abell, R. n. A. Alvarez-Puebla and L. M. Liz-Marzán, *J. Phys. Chem. Lett.*, 2013, **5**, 73–79.
3 C. Zhao, Y. Liu, J. Yang and J. Zhang, *Nanoscale*, 2014, **6**, 9103–9109.
4 J. Zhao, C. Zhang, P. V. Braun and H. Giessen, *Adv. Mater.*, 2012, **24**, OP247–OP252.
5 Z. Zhang, M. Sun, P. Ruan, H. Zheng and H. Xu, *Nanoscale*, 2013, **5**, 4151–4155.
6 H. Wei and H. Xu, *Nanoscale*, 2013, **5**, 10794–10805.
7 C. Zhao, J. Zhang and Y. Liu, *EPJ Appl. Metamater.*, 2014, **1**, 6.
8 C. Zhao, Y. Liu, Y. Zhao, N. Fang and T. J. Huang, *Nat. Commun.*, 2013, **4**, 2305.
9 S. Schietinger, M. Barth, T. Aichele and O. Benson, *Nano Lett.*, 2009, **9**, 1694–1698.
10 J. R. Lakowicz, *Anal. Biochem.*, 2005, **337**, 171–194.
11 L. Zhao, T. Ming, H. Chen, Y. Liang and J. Wang, *Nanoscale*, 2011, **3**, 3849–3859.
12 Y. Cui, K. H. Fung, J. Xu, H. Ma, Y. Jin, S. He and N. X. Fang, *Nano Lett.*, 2012, **12**, 1443–1447.
13 Y. Cui, K. H. Fung, J. Xu, S. He and N. X. Fang, *Opt. Express*, 2012, **20**, 17552–17559.
14 H. Deng, Z. Li, L. Stan, D. Rosenmann, D. Czaplewski, J. Gao and X. Yang, *Opt. Lett.*, 2015, **40**, 2592–2595.
15 M. J. Rozin, D. A. Rosen, T. J. Dill and A. R. Tao, *Nat. Commun.*, 2015, **6**, 7325.
16 J. Henzie, M. H. Lee and T. W. Odom, *Nat. Nanotechnol.*, 2007, **2**, 549–554.

17 N. Zhang, K. Liu, Z. Liu, H. Song, X. Zeng, D. Ji, A. Cheney, S. Jiang and Q. Gan, *Adv. Mater. Interfaces*, 2015, **2**, 1500142.
18 X. Wei, M. Altissimo, T. J. Davis and P. Mulvaney, *Nanoscale*, 2014, **6**, 5372–5377.
19 M. Dulle, S. Jaber, S. Rosenfeldt, A. Radulescu, S. Förster, P. Mulvaney and M. Karg, *Phys. Chem. Chem. Phys.*, 2015, **17**, 1354–1367.
20 F. Cheng, J. Gao, L. Stan, D. Rosenmann, D. Czaplewski and X. Yang, *Opt. Express*, 2015, **23**, 14552–14560.
21 H. Zhu, H. Chen, J. Wang and Q. Li, *Nanoscale*, 2013, **5**, 3742–3746.
22 L. Shao, Q. Ruan, R. Jiang and J. Wang, *Small*, 2014, **10**, 802–811.
23 J. You, X. Li, F.-x. Xie, W. E. I. Sha, J. H. W. Kwong, G. Li, W. C. H. Choy and Y. Yang, *Adv. Energy Mater.*, 2012, **2**, 1203–1207.
24 H. A. Atwater and A. Polman, *Nat. Mater.*, 2010, **9**, 205–213.
25 C. Fang, H. Jia, S. Chang, Q. Ruan, P. Wang, T. Chen and J. Wang, *Energy Environ. Sci.*, 2014, **7**, 3431–3438.
26 A. Pors, M. G. Nielsen and S. I. Bozhevolnyi, *Nano Lett.*, 2015, **15**, 791–797.
27 H. Wei, Z. Wang, X. Tian, M. Käll and H. Xu, *Nat. Commun.*, 2011, **2**, 387.
28 D. Pan, H. Wei and H. Xu, *Opt. Express*, 2013, **21**, 9556–9562.
29 V. R. Shrestha, S.-S. Lee, E.-S. Kim and D.-Y. Choi, *Nano Lett.*, 2014, **14**, 6672–6678.
30 M. Park, C. Harrison, P. M. Chaikin, R. A. Register and D. H. Adamson, *Science*, 1997, **276**, 1401–1404.
31 Y. B. Zheng, B. K. Juluri, X. Mao, T. R. Walker and T. J. Huang, *J. Appl. Phys.*, 2008, **103**, 014308.
32 K. Chen, S. V. Stoianov, J. Bangerter and H. D. Robinson, *J. Colloid Interface Sci.*, 2010, **344**, 315–320.
33 T. R. Jensen, M. D. Malinsky, C. L. Haynes and R. P. Van Duyne, *J. Phys. Chem. B*, 2000, **104**, 10549–10556.
34 J. Zhao, S. Jaber, P. Mulvaney, P. V. Braun and H. Giessen, *Adv. Opt. Mater.*, 2015, **3**, 680–686.
35 A. Nemiroski, M. Gonidec, J. M. Fox, P. Jean-Remy, E. Turnage and G. M. Whitesides, *ACS Nano*, 2014, **8**, 11061–11070.
36 K. Chen, B. B. Rajeeva, Z. Wu, M. Rukavina, T. D. Dao, S. Ishii, M. Aono, T. Nagao and Y. Zheng, *ACS Nano*, 2015, **9**, 6031–6040.
37 S. M. Lubin, A. J. Hryn, M. D. Huntington, C. J. Engel and T. W. Odom, *ACS Nano*, 2013, **7**, 11035–11042.
38 C. D'Andrea, J. Bochterle, A. Toma, C. Huck, F. Neubrech, E. Messina, B. Fazio, O. M. Maragò, E. Di Fabrizio, M. Lamy de La Chapelle, P. G. Gucciardi and A. Pucci, *ACS Nano*, 2013, **7**, 3522–3531.
39 F. Le, D. W. Brandl, Y. A. Urzhumov, H. Wang, J. Kundu, N. J. Halas, J. Aizpurua and P. Nordlander, *ACS Nano*, 2008, **2**, 707–718.
40 N. A. Hatab, C.-H. Hsueh, A. L. Gaddis, S. T. Retterer, J.-H. Li, G. Eres, Z. Zhang and B. Gu, *Nano Lett.*, 2010, **10**, 4952–4955.
41 M. Chirumamilla, A. Toma, A. Gopalakrishnan, G. Das, R. P. Zaccaria, R. Krahne, E. Rondanina, M. Leoncini, C. Liberale, F. De Angelis and E. Di Fabrizio, *Adv. Mater.*, 2014, **26**, 2353–2358.
42 V. Flauraud, T. S. van Zanten, M. Mivelle, C. Manzo, M. F. Garcia Parajo and J. Brugger, *Nano Lett.*, 2015, **15**, 4176–4182.
43 Y. Chu, M. G. Banaee and K. B. Crozier, *ACS Nano*, 2010, **4**, 2804–2810.

